


NANO EXPRESS

Open Access



# TiO<sub>2</sub> Nanomembranes Fabricated by Atomic Layer Deposition for Supercapacitor Electrode with Enhanced Capacitance

Farah Naeem<sup>1,2</sup>, Sumayyah Naeem<sup>1,2</sup>, Yuting Zhao<sup>1</sup>, Dingrun Wang<sup>1</sup>, Jing Zhang<sup>3</sup>, YongFeng Mei<sup>1</sup> and Gaoshan Huang<sup>1\*</sup> 

## Abstract

TiO<sub>2</sub> is a promising environment friendly, low cost, and high electrochemical performance material. However, impediments like high internal ion resistance and low electrical conductivity restrict its applications as electrode for supercapacitor. In the present work, atomic layer deposition was used to fabricate TiO<sub>2</sub> nanomembranes (NMs) with accurately controlled thicknesses. The TiO<sub>2</sub> NMs were then used as electrodes for high-performance pseudocapacitors. Experimental results demonstrated that the TiO<sub>2</sub> NM with 100 ALD cycles had the highest capacitance of 2332 F/g at 1 A/g with energy density of 81 Wh/kg. The enhanced performance was ascribed to the large surface area and the interconnectivity in the case of ultra-thin and flexible NMs. Increased ALD cycles led to stiffer NMs and decreased capacitance. Moreover, one series of two supercapacitors can light up one light-emitting diode with a working voltage of ~ 1.5 V, sufficiently describing its application values.

**Keywords:** Atomic layer deposition, TiO<sub>2</sub> nanomembranes, Electrode, Supercapacitor

## Introduction

With the maturation of energy storage technology [1], supercapacitors have received vast attention due to their high power density, fast charge-discharge rate, and good cycling performance [2–4]. Pseudocapacitor is an important class of supercapacitors, which can deliver attractive high capacitance and energy density compared with electrochemical supercapacitors [5–7]. In the past few decades, the transition metal oxides (e.g., RuO<sub>2</sub> [8], MoO<sub>2</sub> [9], MnO<sub>2</sub> [10], Ni/NiO [11], Co<sub>3</sub>O<sub>4</sub> [12], and TiO<sub>2</sub> [13]) and hydroxides [14–16] were used as classic electrode materials for pseudocapacitors owing to low cost, low toxicity, multiple oxidation states [17], and great flexibility in structures and morphology. However, their thermal instability, impurity defects, and rate capability are usually limited by the inadequate conductivity to support fast electron transport required by high rates. In order to solve these problems, low-dimensional TiO<sub>2</sub> structures (1D, 2D, 2D + 1D, and 3D) with high surface-to-volume

ratio, good surface structure, great electrical and thermal stability, favorable energy band gap properties, and high dielectric constant have been engaged as promising electrode materials for supercapacitors [18–22]. Especially, we think that 2D nanomembrane (NM) structures with excellent flexibility should have great potential in electrode applications. The thickness control of nanomembrane is therefore crucial in fabricating functional devices in well-defined nanoworld [23]. In addition, large-scale manufacturing of nanoscale materials is also crucial for practical applications [24]. One may note that atomic layer deposition (ALD) is a captivating technique used to construct nanodevices [25, 26]. This powerful technique can deposit thin films layer by layer with accurate thickness control and can conformally cover 3D structures with high aspect ratio [27–30], and the productivity can thus be greatly enhanced. In the current work, we present the fabrication of 2D TiO<sub>2</sub> NMs with different thicknesses by performing ALD on 3D porous polymer template with large surface area [31, 32]. Microstructural characterization elucidates that the crystal structure of NM is a mixture of anatase and rutile phases. Electrochemical characterizations demonstrate that the ultra-thin and flexible

\* Correspondence: [gshuang@fudan.edu.cn](mailto:gshuang@fudan.edu.cn)

<sup>1</sup>Department of Materials Science, Fudan University, 220 Handan Road, Shanghai 200433, People's Republic of China

Full list of author information is available at the end of the article

NMs have the enhanced performance due to the large surface area and the interconnectivity among the NMs. The improved ion transportation causes Faradaic reaction on the surface as well as in the bulk [33], resulting in increased capacitance and energy densities.

## Methods

### Fabrication of TiO<sub>2</sub> NMs

TiO<sub>2</sub> NMs with various thicknesses (100, 200, and 400 ALD cycles) were deposited on a commercially available polyurethane sponge by using ALD technique. Tetraakis dimethylamide titanium (TDMAT) and de-ionized (DI) water were used as precursors in the presence of nitrogen (N<sub>2</sub>) gas which served as both carrier and purge gases. The flow rate of the carrier gas was 20 sccm. A typical ALD sequence includes TDMAT pulse (200 ms), N<sub>2</sub> purge (20,000 ms), H<sub>2</sub>O pulse (20 ms), and N<sub>2</sub> purge (30,000 ms). The precursors used were purchased from J&K Scientific Ltd., China. The precursor conformally covered the three-dimensionally porous sponge, which led to promoted productivity due to the large surface area of the template [34]. The TiO<sub>2</sub>-coated sponges were calcinated at 500 °C for 4 h in an O<sub>2</sub> flow of 400 mL/min, and the template was completely removed. The resultant TiO<sub>2</sub> NMs were crushed and cleaned in ethanol, hydrochloric acid (HCl), and DI water.

### Preparation of Electrode

In order to fabricate high-performance supercapacitor, TiO<sub>2</sub> NMs with 100, 200, and 400 ALD cycles were used as the active material and polytetrafluoroethylene (PTFE) was used as binder. The contents of TiO<sub>2</sub> NMs and binder were 90 wt% and 10 wt%, respectively. A homogeneous TiO<sub>2</sub> NMs slurry was obtained by mixing the NMs and binder with a small quantity of ethanol, and a milling process was engaged. The prepared uniform slurry was deposited onto the cleaned nickel foam and then the sample was degassed at 60 °C for 2 h in vacuum. In order to complete the electrode fabrication, the sample was pressed under 10 MPa pressure. The prepared TiO<sub>2</sub> NMs electrode was soaked in 1 M KOH solution for 12 h to activate the electrode. The loading densities of active materials were about ~ 1.5 mg cm<sup>-2</sup> for all electrodes. The mass of the TiO<sub>2</sub> NMs on nickel foam was obtained by calculating the mass difference between the electrode and nickel foam [35].

### Microstructural Characterization

The crystallographic structure of the TiO<sub>2</sub> NMs was inspected by X-ray diffraction technique (XRD). The XRD patterns were recorded by using a Bruker D8A Advanced XRD with Cu K $\alpha$  radiation ( $\lambda = 1.5405 \text{ \AA}$ ). The morphology of TiO<sub>2</sub> NMs was examined by scanning electron microscopy (SEM, Zeiss Sigma). The Raman

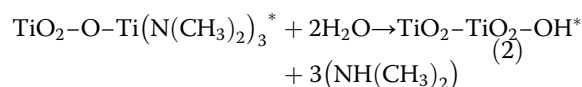
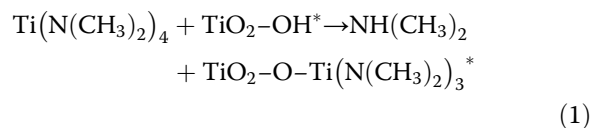
spectra of the samples were carried out on a Horiba Scientific Raman spectrometer ( $\lambda = 514 \text{ nm}$ ). The elemental analysis and chemical state of the TiO<sub>2</sub> NMs were obtained by using a PHI 5000C EACA X-ray photoelectron spectroscope (XPS), with C 1s peak at 284.6 eV as the standard signal. Atomic force microscopy (AFM, Dimension Edge, Bruker, USA) with tapping mode was used for surface topography of TiO<sub>2</sub> NMs.

### Electrochemical Characterization

Three-electrode system was utilized to study the electrochemical properties of the TiO<sub>2</sub> NMs working electrode where Ag/AgCl and platinum foil were acted as a reference electrode and counter electrode, respectively. The cyclic voltammetry (CV), chronopotentiometry (CP), and electrochemical impedance spectroscopy (EIS) measurements were accomplished on a Chenhua CHI 660E electrochemical workstation at 25 °C in 1 M KOH aqueous solution. EIS results were obtained over the frequency range of 100 KHz to 1 Hz with an amplitude of 5 mV. The calculation methods of specific capacitances and energy/power densities are described in Additional file 1.

## Results and Discussion

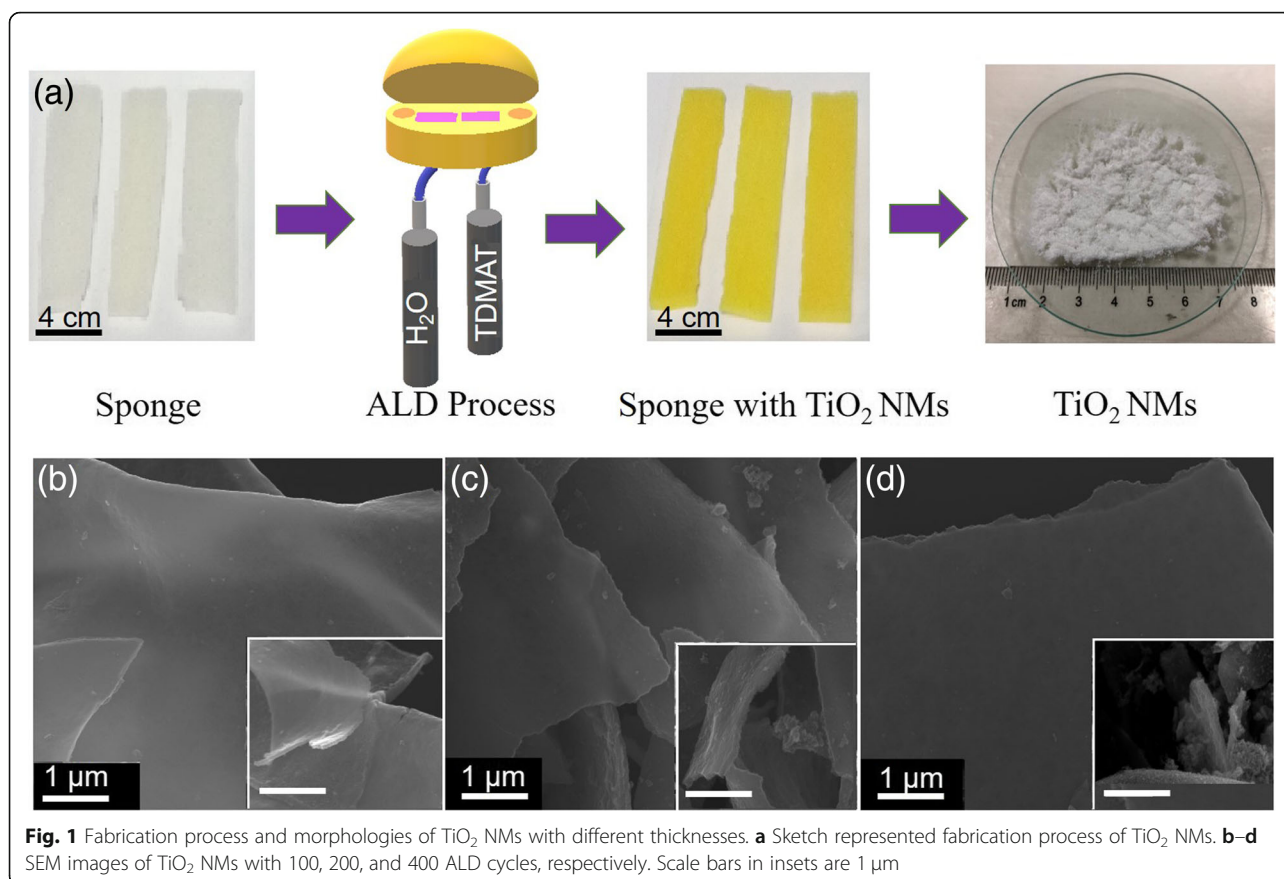
The preparation of TiO<sub>2</sub> NMs is shown in Fig. 1a. The TDMAT and H<sub>2</sub>O were used as ALD precursors to deposit TiO<sub>2</sub> on polyurethane sponge template. The reaction can be described in two half equations as follows: [36]



The total reaction can be written as:



The sponge with TiO<sub>2</sub> NM coated was then heated to high temperature. During calcination at 500 °C under oxygen atmosphere, the polymer template was converted into CO<sub>2</sub> and left the 3D porous NM structure behind [34]. Crushing this 3D porous structure led to the fabrication of powder-like structure in white (Fig. 1a). The morphologies of TiO<sub>2</sub> NMs with 100, 200, and 400 ALD cycles were further observed by SEM and are demonstrated in Fig. 1b–d. We found the lateral sizes of the NMs with different ALD cycles are typically around tens of microns. The thickness of TiO<sub>2</sub> NMs fabricated in this work was probed by AFM technique and the results are presented in Additional file 1: Figure S1. The average



thickness of TiO<sub>2</sub> NMs with 100, 200, and 400 ALD cycles are ~ 15, 34, and 71 nm, respectively. With the increase of ALD cycles, TiO<sub>2</sub> NMs is converted into a thicker and stiffer sheet. The corresponding insets in Fig. 1b–d demonstrate that the thickness of NMs is uniform, and some small creases represent the flexibility of TiO<sub>2</sub> NM especially in the thinner cases. The NMs deposited by ALD can replicate the morphology of the original substrate (i.e., sponge) and therefore some irregular surface structures in the insets of Fig. 1c and d may originate from the template or from the calcination process [37]. Normally, TiO<sub>2</sub> has three different crystal structures: anatase (tetragonal; space group, *I41/amd*), brookite (orthorhombic; space group, *Pcab*), and rutile (tetragonal; space group, *P42/mnm*) phases. Here, we carried out detailed characterization to investigate the microstructural properties of TiO<sub>2</sub> NMs. The crystal structures of the TiO<sub>2</sub> NMs were investigated by XRD, and the corresponding results are shown in Fig. 2a. The diffraction peaks are indexed to TiO<sub>2</sub> with anatase and rutile structures (see Additional file 1: Figure S2), indicating the existence of the mixture phase in TiO<sub>2</sub> NMs calcinated at 500 °C. The co-existence of both phases could be valuable for supercapacitor performance of TiO<sub>2</sub> NMs [30, 38]. Figure 2b further demonstrates the

Raman spectra of corresponding TiO<sub>2</sub> NMs, which can also be used to identify the phases existed in the NMs. Here, five Raman peaks ascribed to anatase TiO<sub>2</sub> are located at ~ 142 (E<sub>g</sub>), 393 (B<sub>1g</sub>), 397 (B<sub>1g</sub>), 513 (A<sub>1g</sub>), 515 (A<sub>1g</sub>), and 634 (E<sub>g</sub>) cm<sup>-1</sup> [39], and they can be observed in all three samples. On the other hand, the 445 cm<sup>-1</sup> (E<sub>g</sub>) peak is connected with rutile phase and can be seen in all three samples but the Raman peak at 610 cm<sup>-1</sup> (A<sub>1g</sub>) appears only in TiO<sub>2</sub> NM with 400 ALD cycles [40]. The emergence of 610 cm<sup>-1</sup> (A<sub>1g</sub>) peak reflects the microstructural change, which might be caused by the insufficient oxygen for the thick NM during heat treatment in oxygen [41]. This indicates that the increased number of ALD cycles has a remarkable influence on the crystal structure of the TiO<sub>2</sub> NMs, which can be probed by XRD and Raman spectra shown in Fig. 2. The electronic configuration of the TiO<sub>2</sub> NMs was also studied by XPS and the results are displayed in Additional file 1: Figure S3. The results prove the existence of Ti<sup>4+</sup> in all NMs and a small shift of the peaks may be ascribed to the change in crystal structure as mentioned above. In order to study the electrochemical performance of the TiO<sub>2</sub> NMs, three-electrode electrochemical system including a reference electrode, counter electrode, and a working electrode was operated. Here, Ag/AgCl was

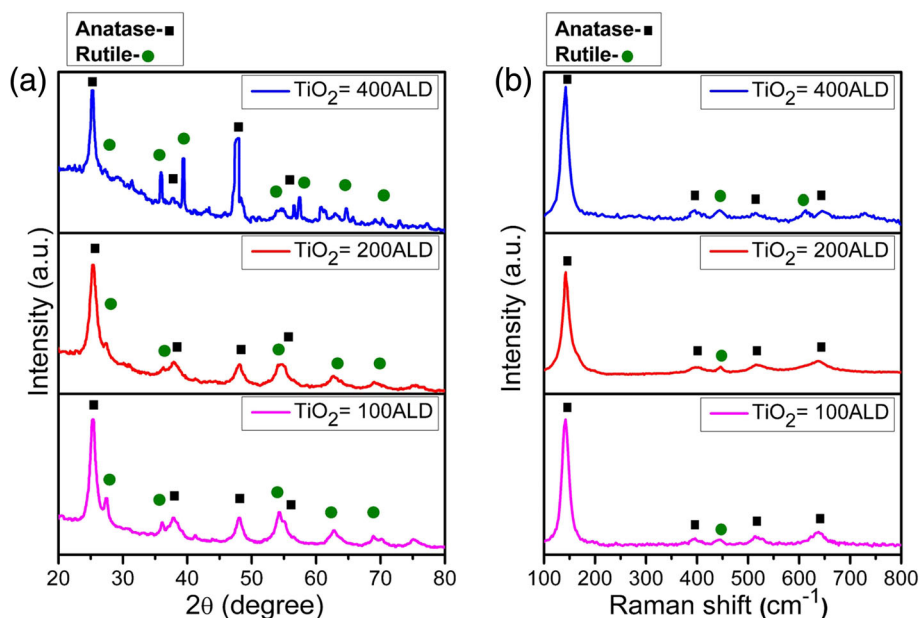
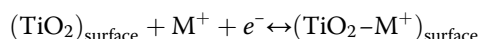


**Fig. 2** Micro-structural characterizations of TiO<sub>2</sub> NMs. **a** XRD patterns of TiO<sub>2</sub> NMs fabricated with 100, 200, and 400 ALD cycles. **b** Raman spectra of TiO<sub>2</sub> NMs fabricated with 100, 200, and 400 ALD cycles

served as a reference electrode to control the potential difference and Pt counter electrode was engaged as an electron source to transit current towards TiO<sub>2</sub> NMs working electrode in the presence of aqueous electrolyte (1 M KOH solution). It is worth noting that the functional voltage of supercapacitor depends on the electrolyte, and aqueous electrolyte with well electronic conductivity and high dielectric constant may be helpful in attaining higher capacitance [42]. The acquired CV and CP curves of electrodes made from TiO<sub>2</sub> NMs with 100, 200, and 400 ALD cycles are displayed in Fig. 3a, b and Additional file 1: Figure S4. One can see that in Fig. 3a, all CV curves of three electrodes made from TiO<sub>2</sub> NMs with different thicknesses exhibit redox peaks. The CV curve of pure nickel foam is also plotted for comparison, and no obvious peak can be observed. Generally, the appearance of redox peaks can be associated to cation interactions on the surface of the TiO<sub>2</sub> NMs, and the interaction can be expressed as: [43]



where M<sup>+</sup> could be H<sub>3</sub>O<sup>+</sup> or K<sup>+</sup> in the electrolyte. The change between different oxidation states of Ti ion suggests its potential as redox electrode material. In response of fast surface Farad reaction, the CV curves of TiO<sub>2</sub> NMs exhibit larger areas compared with that of pure Ni-foam, implying the higher specific capacitance value of TiO<sub>2</sub> NMs. Specifically, one can see the area of the CV curves decreases with the ALD cycles, suggesting

a decrease of capacitance in the case of thicker NMs, as will be further proved in following CP results. A reduction peak at ~0.2 V can be clearly observed in all the electrodes and is associated with intraband gap localized states [44, 45]. In addition, we also measured CV curves of electrode made from TiO<sub>2</sub> NMs with 100 ALD at different scan rates, and the results are shown in Fig. 3b. A redox peak shifting behavior (from higher to lower potential) is connected with the change in intercalation/deintercalation of M<sup>+</sup> ions and synergetic effect [46, 47]. Briefly, limited diffusion and charge transfer rate at a higher scan rate lead to corresponding shift [48, 49]. In order to further illustrate the charging/discharging behavior, the galvanostatic charge/discharge curves of TiO<sub>2</sub> NMs electrodes at different current densities within a potential range of 0–0.5 V are shown in Fig. 3c, d and Additional file 1: Figure S4. The nonlinear curves of CP represent the pseudocapacitor function, which is consistent with the CV curves, and represent the Faradaic behavior. It should be noted that the discharge time of TiO<sub>2</sub> NMs electrode with 100 ALD cycles is notably prolonged compared with TiO<sub>2</sub> NMs electrodes with 200 and 400 ALD cycles, indicating the largest specific capacitance value. However, ultra-thin NMs electrode exhibit high gravimetric specific activity but cannot afford large current due to the limited number of active sites [50]. The extended charging/discharging times of TiO<sub>2</sub> NMs electrodes with 100, 200, and 400 ALD cycles at current density of 1 A/g means that reduction/oxidation reactions take place (mainly on surfaces of NMs) during the process, which is the property of pseudocapacitor [51].



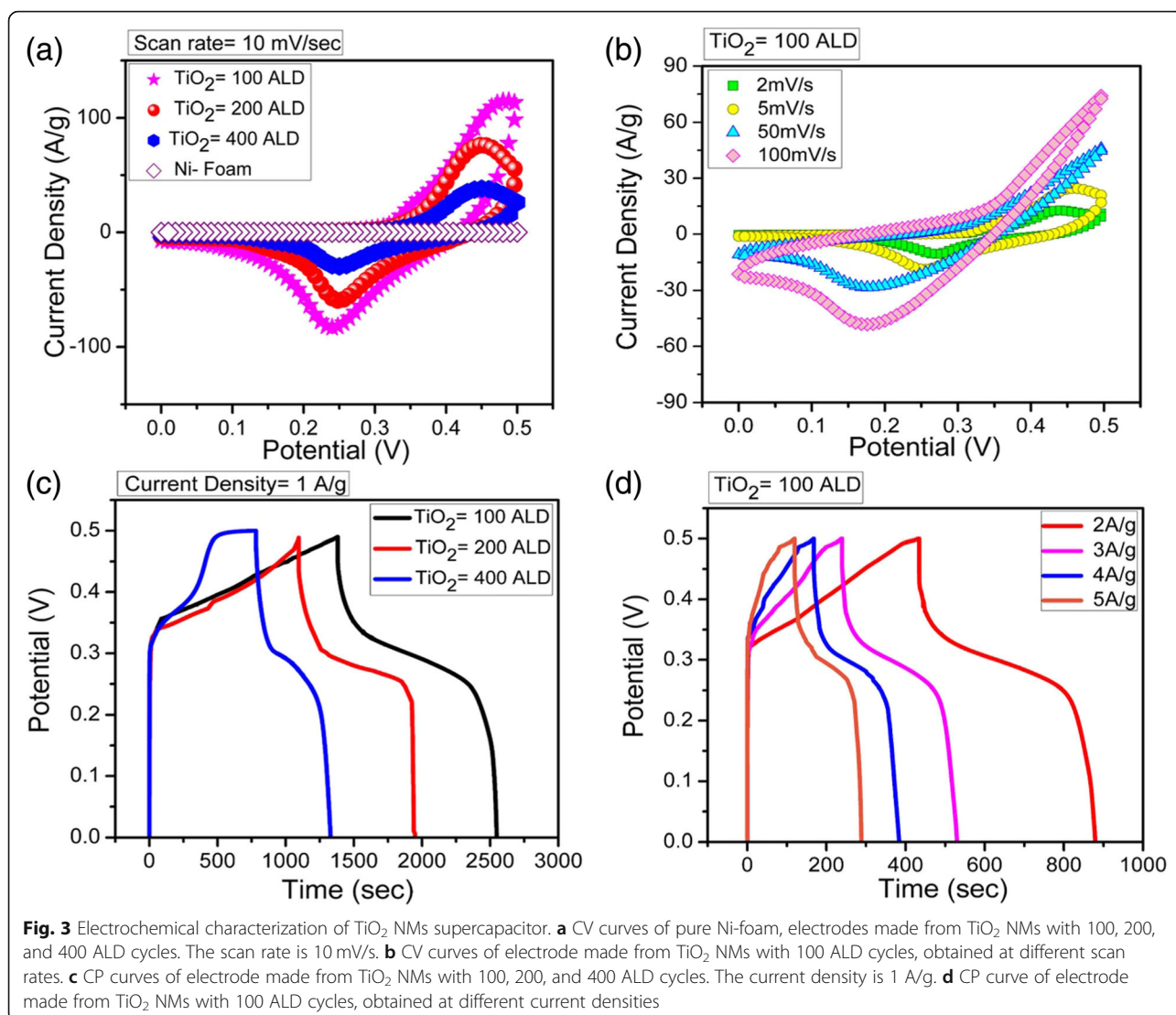
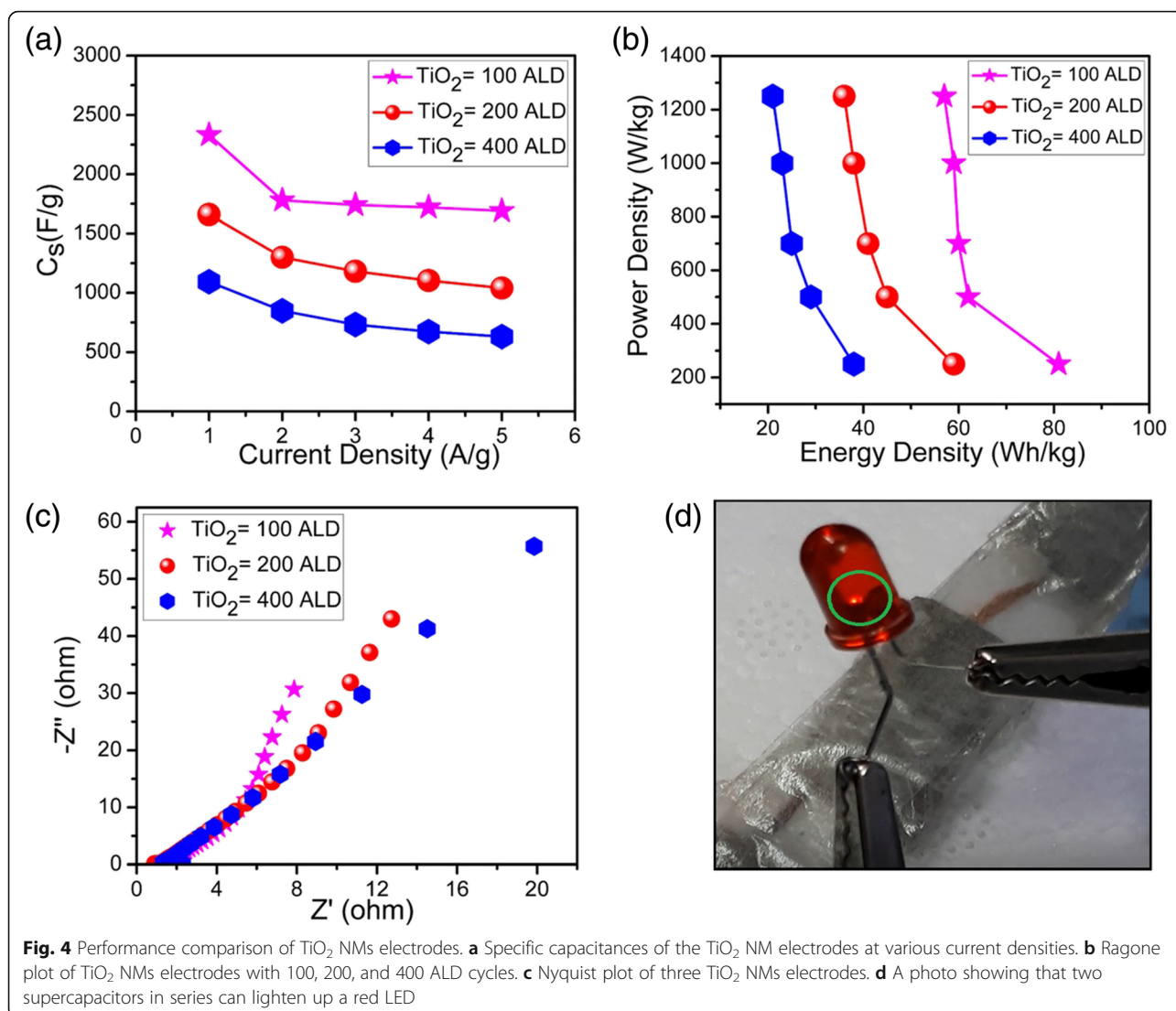


Figure 4 (a) shows the specific capacitances of electrodes made from TiO<sub>2</sub> NMs with 100, 200, and 400 ALD cycles at different current densities ranging from 1 to 5 A/g. Specific capacitances of 2332, 1780, 1740, 1720, and 1690 F/g are obtained from TiO<sub>2</sub> NMs with 100 ALD cycles, 1660, 1300, 1182, 1104, and 1040 F/g from TiO<sub>2</sub> NMs with 200 ALD, and 1094, 848, 732, 672, and 630 F/g from TiO<sub>2</sub> NMs with 400 ALD cycles. In previous literature, Yang et al. [43] prepared the TiO<sub>2</sub>/N-doped graphene composite structure with a capacitance of 385.2 F/g at 1 A/g and 320.1 F/g at 10 A/g. Zhi et al. [52] reported a specific capacitance of 216 F/g for TiO<sub>2</sub> nanobelts with nitrogen doping. Di et al. [53] fabricated TiO<sub>2</sub> nanotubes decorated with MnO<sub>2</sub> nanoparticles and a specific capacitance of 299 F/g at a current density of 0.5 A/g was obtained. Obviously, the capacitance of the electrode made from current TiO<sub>2</sub> NMs is much higher. Moreover, the energy and power density relation of the three electrodes are shown

in Fig. 4b and Additional file 1: Table S1. Energy density is the capacity of energy storage devices and power density is their ability to deliver it, and both are the key parameters used to evaluate the electrochemical performance of supercapacitors. Vividly, when current density increases from 1 to 5 A/g, TiO<sub>2</sub> NMs electrode with 100 ALD cycles possesses a high energy density of 81–57 Wh/kg compared to 59–36 Wh/kg of TiO<sub>2</sub> NMs electrode with 200 ALD cycles and 38–21 Wh/kg of TiO<sub>2</sub> electrode NMs with 400 ALD cycles, while the power density increases from 250 to 1250 W/kg (Fig. 4b). The high performance might be due to the mixture of anatase and rutile phases (Fig. 2) as this leads to surface passivation and increased ion transportation [54–56]. In addition, the enlarged surface area of the TiO<sub>2</sub> NMs and interconnectivity among the NMs also cause the enhancement in ions transportation. On the other hand, we believe that the decrease in electrochemical performance with the increasing ALD



**Fig. 4** Performance comparison of  $\text{TiO}_2$  NMs electrodes. **a** Specific capacitances of the  $\text{TiO}_2$  NM electrodes at various current densities. **b** Ragone plot of  $\text{TiO}_2$  NMs electrodes with 100, 200, and 400 ALD cycles. **c** Nyquist plot of three  $\text{TiO}_2$  NMs electrodes. **d** A photo showing that two supercapacitors in series can light up a red LED

cycles is mainly due to the decreased NM/electrolyte interface area if the masses of the active materials are the same. Moreover, the  $\text{TiO}_2$  NMs with more ALD cycles (i.e., thickness) is stiffer and flat (see Fig. 1), and therefore, the overlap between the NMs is obvious. This may limit the surface access for electrolyte ions, resulting in dead volume, high resistance, and reduced capacitance [57]. In addition, with the increase of current densities, the diffusion rate of electrolyte might not be enough to satisfy the electrochemical reaction of electrode material, and therefore, a decrease of capacitance with current density can be observed in Fig. 4a [39, 40]. In order to further reveal the electrochemical properties of the current  $\text{TiO}_2$  NMs electrodes, EIS characterizations was carried out because EIS can provide the information about electrode-electrolyte and electrode internal resistance [58]. Figure 4c demonstrates the EIS results of all three electrodes, and the horizontal intercept indicates the internal resistance of

pseudocapacitor. It is clearly observed that  $\text{TiO}_2$  NMs electrode with 400 ALD cycles possesses high internal resistance as compared to  $\text{TiO}_2$  NMs electrodes with 200 and 100 ALD cycles. We consider that the increased resistance of  $\text{TiO}_2$  NMs electrode with 400 ALD cycles is mostly by reason of increased NM thickness since the  $\text{TiO}_2$  has relatively large resistivity [39, 48]. The  $\text{TiO}_2$  NMs with 100 ALD cycles exhibits the lowest internal resistance compared with others because the large surface area allows the better ions passage [59] and flexibility of thin NM improves the interlayer connection with decreased resistivity. All these results demonstrate that thin  $\text{TiO}_2$  NMs with high electroactivity are promising electrode materials for high-performance pseudocapacitor. In order demonstrate the potential application of  $\text{TiO}_2$  NMs supercapacitor, four electrodes made from  $\text{TiO}_2$  NMs with 100 ALD cycles were assembled into two symmetrical supercapacitors, i.e., each supercapacitor consisted of two

electrodes of TiO<sub>2</sub> NMs with 100 ALD cycles. The two supercapacitors were connected in series and then charged at 5 A/g current density to 0.5 V. Afterwards, they were used to light up a red LED (light-emitting diode) with working voltage of ~1.5 V and the LED emitted light for ~1 min (see Fig. 4d and Additional file 2: Video S1). The cycle stability of the electrode made from TiO<sub>2</sub> NMs with 100 ALD cycles was also studied and the results are shown in Additional file 1: Figure S5. A capacitance retention of 80.98% is observed after cycling at 5 A/g for 40 charge/discharge cycles, suggesting a less interaction of electrolyte ions with electrode surface after repeated cycles. We believe that the performance of the NMs electrode might be further promoted if the conductivity of the NMs is increased. With the help of the ALD technique, the conductivity of the NMs can be increased by fabricating multi-layered NMs where materials with high conductivity are incorporated. More works are currently in progress.

## Conclusion

In summary, we have fabricated TiO<sub>2</sub> NMs for electrodes of supercapacitor, and the electrochemical performance of the NMs was studied in detail. The TiO<sub>2</sub> NM electrode demonstrates increased capacitance with decreased NM thickness. At a current density of 1 A/g, the specific capacitance of 2332 F/g is obtained for TiO<sub>2</sub> NM with 100 ALD cycles, and the corresponding energy density is calculated to be 81 Wh/kg. The enhancement of the performance is mainly attributed to the fabrication strategy and the ultra-thin feature of NMs, because the large surface area and short diffusion path of NMs facilitate ion transport through electrode/electrolyte interface. The interconnectivity among the NMs also remarkably enhances the ion transportation in the electrode. We also demonstrate that two supercapacitors connected in series can power a LED, suggesting the application potential of TiO<sub>2</sub> NMs supercapacitor. The current facile design opens the way to build NMs electrodes for next-generation wearable energy storage devices at low-cost. However, for practical applications of NM-based structures in future supercapacitors, further studies are required.

## Additional files

**Additional file 1: Figure S1.** Surface morphologies of ALD synthesized TiO<sub>2</sub> NMs with different ALD cycles: (a) 100 ALD cycles. (b) 200 ALD cycles. (c) 400 ALD cycles. **Figure S2.** Crystal structures of TiO<sub>2</sub>. (a) Diagram showing the arrangement of atoms in anatase and rutile phases of TiO<sub>2</sub>. (b) Standard XRD patterns of anatase TiO<sub>2</sub> (JPCDS # 21-1272) and rutile TiO<sub>2</sub> (JPCDS # 03-1122). **Figure S3.** XPS spectra of TiO<sub>2</sub> NMs with 100, 200, and 400 ALD cycles. To calibrate, C 1s peak is used as reference peak at binding energy of 284.6 eV. High-resolution XPS spectra of (a) Ti 2p and (b) O 1s. The peaks at ~464.9 and ~459 eV is assigned to Ti<sup>4+</sup> 2p<sub>1/2</sub> and Ti<sup>4+</sup> 2p<sub>3/2</sub> respectively. The peak at 529 eV is assigned to O 1s. **Figure S4.** Electrochemical characterization of TiO<sub>2</sub> NMs. (a) and (c) CV curves of TiO<sub>2</sub> NMs with 200 and 400 ALD cycles at different scan rates.

(b) and (d) CP curves of TiO<sub>2</sub> NMs with 200 and 400 ALD cycles at different current densities. **Figure S5.** Cycle performance of electrode made from TiO<sub>2</sub> NMs with 100 ALD cycles. **Table S1.** Comparison of specific capacitance and energy density of electrodes made from TiO<sub>2</sub> NMs with different ALD cycles. (DOCX 2102 kb)

**Additional file 2: Video S1.** Two supercapacitors in series can lighten up a red LED. (MP4 1136 kb)

## Abbreviations

AFM: Atomic force microscopy; ALD: Atomic layer deposition; CP: Chronopotentiometry; CV: Cyclic voltammetry; DI: De-ionized water; EIS: Electrochemical impedance spectroscopy; LED: Light-emitting diode; NMs: Nanomembranes; PTFE: Polytetrafluoroethylene; SEM: Scanning electron microscopy; TDMAT: Tetrakis dimethylamide titanium; XPS: X-ray photoelectron spectroscopy; XRD: X-ray diffraction spectrometer

## Acknowledgement

The authors are grateful to Dr. Yingchang Jiang, Zhao Zhe, Dr. Atif Zahoor, Dr. Shahid Rasool, Dr. Alexander A Solovov and Dr. David H. Gracias for their helpful discussion and guidance.

## Funding

This work is supported by the Natural Science Foundation of China (Nos. U1632115 and 61805042), Science and Technology Commission of Shanghai Municipality (No. 17JC1401700), and the Changjiang Young Scholars Program of China. Part of the work is also supported by the National Key Technologies R&D Program of China (No. 2015ZX02102-003).

## Availability of Data and Materials

The datasets generated during and/or analyzed during the current study are available from the corresponding author on request.

## Authors' Contributions

FN carried out the experiment, analyzed the data, and wrote the manuscript. SN helped in analyzing the data. YTZ and DRW helped in the sample characterization. JZ, YFM, and GSH provided the research directions and revised the manuscript. All authors read and approved the final manuscript.

## Competing Interests

The authors declare that they have no competing interests.

## Publisher's Note

Springer Nature remains neutral with regard to jurisdictional claims in published maps and institutional affiliations.

## Author details

<sup>1</sup>Department of Materials Science, Fudan University, 220 Handan Road, Shanghai 200433, People's Republic of China. <sup>2</sup>State Key Laboratory for Modification of Chemical Fibers and Polymer Material Science and Engineering, Donghua University, Shanghai 201620, People's Republic of China. <sup>3</sup>College of Science, Donghua University, Shanghai 201620, People's Republic of China.

Received: 28 December 2018 Accepted: 25 February 2019

Published online: 13 March 2019

## References

1. Armaroli N, Balzani V (2011) Towards an electricity-powered world. *Energy Environ Sci* 4:3193–3222
2. Yu M, Han Y, Cheng X, Hu L, Zeng Y, Chen M, Cheng F, Lu X, Tong Y (2015) Holey tungsten oxynitride nanowires: novel anodes efficiently integrate microbial chemical energy conversion and electrochemical energy storage. *Adv Mater* 27:3085–3091
3. Kötz R, Carlen M (2000) Principles and applications of electrochemical capacitors. *Electro Acta*. 45:2483
4. Burke A (2000) Ultracapacitors: why, how, and where is the technology. *J Power Sources* 91:37
5. Conway BE, Birss V, Wojtowicz J (1997) The role and utilization of pseudocapacitance for energy storage by supercapacitors. *J Power Sources* 66:1–14

6. Miller J, R Simon P (2008) Electrochemical capacitors for energy management. *Science* 321:651–652
7. Meng X, Deng J, Zhu J, Bi H, Kan E, Wang X (2016) Cobalt sulfide/graphene composite hydrogel as electrode for high-performance pseudocapacitors. *Sci Rep* 6:21717–21725
8. Trasatt S, Buzzancai G (1971) Ruthenium dioxide: a new interesting electrode material. Solid state structure and electrochemical behaviour. *J Electroanal Chem* 29:A1–A5
9. Yao B, Huang L, Zhang J, Gao X, Wu J, Cheng Y, Xiao X, Wang B, Li Y, Zhou J (2016) Flexible transparent molybdenum trioxide nanopaper for energy storage. *Adv Mater* 28:6353–6358
10. Huang ZH, Song Y, Feng DY, Sun Z, Sun XQ, Liu XX (2018) High mass loading MnO<sub>2</sub> with hierarchical nanostructures for supercapacitors. *ACS Nano* 12:3557–3567
11. Liu FG, Wang XB, Hao J, Han S, Lian J, Jiang Q (2017) High density arrayed Ni/NiO core-shell nanospheres evenly distributed on graphene for ultrahigh performance supercapacitor. *Sci Rep* 7:17709–17718
12. Duan Y, Hu T, Yang L, Gao J, Guo S, Hou M, Ye X (2019) Facile fabrication of electroactive microporous Co<sub>3</sub>O<sub>4</sub> through microwave plasma etching for supercapacitors. *J of Alloys and Comp* 771:156–161
13. Lu X, Wang G, Zhai T, Yu M, Gan J, Tong Y, Li Y (2012) Hydrogenated TiO<sub>2</sub> Nanotube Arrays for Supercapacitors. *Nano Lett* 12:1690–1696
14. Deng T, Lu Y, Zhang W, Sui M, Shi X, Wang D, Zheng W (2018) Inverted design for high-performance supercapacitor via co (OH) 2-derived highly oriented MOF electrodes. *Adv Energy Mat* 8: 1702294–1702300
15. Wang HL, Casalongue HS, Liang Y, Dai HJ (2010) Ni (OH)<sub>2</sub> nanoplates grown on graphene as advanced electrochemical pseudocapacitor materials. *J Am Chem Soc* 132:7472–7477
16. Xia XH, Tu JP, Zhang YQ, Chen J, Wang XL, Gu CD, Guan C, Luo JS, Fan HJ (2012) Porous hydroxide nanosheets on preformed nanowires by electrodeposition: branched nanoarrays for electrochemical energy storage. *Chem Mater* 24:3793–3799
17. Zhao X, Sánchez BM, Dobson PJ, Grant PS (2011) The role of nanomaterials in redox-based supercapacitors for next generation energy storage devices. *Nanoscale* 3:839–855
18. Ozkan S, Nguyen NT, Hwang I, Mazare A, Schmuki P (2017) Highly conducting spaced TiO<sub>2</sub> nanotubes enable defined conformal coating with nanocrystalline Nb<sub>2</sub>O<sub>5</sub> and high-performance supercapacitor applications. *Small* 13:1603821
19. Banerjee AN, Anitha VC, Joo SW (2017) Improved electrochemical properties of morphology controlled titania/titanate nanostructures prepared by in-situ hydrothermal surface modification of self-source Ti substrate for high performance supercapacitors. *Sci Rep* 7:13227–13246
20. Ke QQ, Zheng M, Liu HJ, Guan C, Mao L, Wang J (2015) 3D TiO<sub>2</sub>@Ni (OH)<sub>2</sub> core-shell arrays with tunable nanostructure for hybrid supercapacitor application. *Sci Rep* 5:13940–13950
21. Jiang L, Ren ZF, Chen S, Zhang Q, Lu X, Zhang HP, Guojiang Wan GJ (2018) Bio-derived three-dimensional hierarchical carbon-graphene-TiO<sub>2</sub> as electrode for supercapacitors. *Sci Rep* 8:4412–4120
22. Kim C, Kim S, Lee J, Kim J, Yoon J (2015) Capacitive and oxidant generating properties of black-colored TiO<sub>2</sub> nanotube array fabricated by electrochemical self-doping. *ACS Appl Mater Inter* 7:7486–7491
23. Huang G, Mei YF (2018) Assembly and self-assembly of nanomembrane materials—from 2D to 3D. *Small* 14:1703665
24. Li XJ, Liu W, Wang J, Rozen I, He S, Chen C, Kim GH, Lee HJ, Lee H-B-R, Kwon S-H, Li LT, Li QL, Wang J, Mei YF (2017) Nanoconfined atomic layer deposition of TiO<sub>2</sub>/Pt nanotubes: toward ultrasmall highly efficient catalytic nanorockets. *Adv Funct Mater* 27:1700598
25. George SM (2010) Atomic layer deposition: an overview. *Chem Rev* 110:111–131
26. Johnson RW, Hultqvist A, Bent SF (2014) A brief review of atomic layer deposition: from fundamentals to applications. *Mater Today* 17:236–246
27. George SM, Ott AW, Klaus JW (1996) Surface chemistry for atomic layer growth. *J Phys Chem* 100:13121–13131
28. Ritala M, Leskela M. *Handbook of thin film materials*; Nalwa, H. S., Ed.; Academic Press: San Diego, 2001
29. Kim H (2011) Characteristics and applications of plasma enhanced-atomic layer deposition. *Thin Solid Films* 519:6639–6644
30. Boukhalfa S, Evanoff K, Yushin G (2012) Atomic layer deposition of vanadium oxide on carbon nanotubes for high-power supercapacitor electrodes. *Energy Environ Sci* 5:6872–6879
31. Abendroth B, Moebus T, Rentrop S, Strohmeier R, Vinnichenko M, Weling T, Stöcker H, Meyer DC (2013) Atomic layer deposition of TiO<sub>2</sub> from tetrakis(dimethylamino) titanium and H<sub>2</sub>O. *Thin Solid Films* 545:176–182
32. Reiners M, Xu K, Aslam N, Devi A, Waser R, Eifert SH (2013) Growth and crystallization of TiO<sub>2</sub> thin films by atomic layer deposition using a novel amido guanidinate titanium source and tetrakis-dimethylamido-titanium. *Chem Mater* 25:2934–2943
33. Sun X, Xie M, Wang GK, Sun HT, Cavanagh AS, Travis JJ, George SM, Liana J (2012) Atomic layer deposition of TiO<sub>2</sub> on graphene for supercapacitors. *J of the Electro Soc* 159:364–369
34. Pan SQ, Zhao Y, Huang GS, Wang J, Baunack S, Gemming T, Li ML, Zheng L, Schmidt OG, Mei YF (2015) Highly photocatalytic TiO<sub>2</sub> interconnected porous powder fabricated by sponge-templated atomic layer deposition. *Nanotech*. 26:364001–364006
35. Chen H, Hu LF, Chen M, Yan Y, Wu L (2014) Nickel-cobalt layered double hydroxide nanosheet for high-performers supercapacitor electrode materials. *Adv Funct Mater* 24:934–942
36. Xie Q, Jiang YL, Detavernier C, Deduytsche D, Meirhaeghe RLV, Ru GP, Li BZ, Qu X (2007) Atomic layer atomic layer deposition of TiO<sub>2</sub> from tetrakis-dimethyl-amido titanium or Ti isopropoxide precursors and H<sub>2</sub>O. *J of Appl Phy* 102:083521–083527
37. Edy R, Huang GS, Zhao Y, Zhang J, Mei YF, Shi JJ (2016) Atomic layer deposition of TiO<sub>2</sub>-nanomembrane-based photocatalysts with enhanced performance. *AIP Adv* 6:115113–115121
38. Huang S, Zhang L, Lu X, Liu L, Sun X, Yin Y, Oswald S, Zou Z, Ding F, Schmidt OG (2017) Tunable pseudocapacitance in 3D TiO<sub>2</sub>-δ nanomembranes enabling superior lithium storage performance. *ACS Nano* 11:821–830
39. Salari M, Konstantinov K, Liu HK (2011) Enhancement of the capacitance in TiO<sub>2</sub> nanotubes through controlled introduction of oxygen vacancies. *J Mater Chem* 21:5128–5133
40. Rezaee M, Khoie SMM, Liu KH (2011) The role of brookite in mechanical activation of anatase-to-rutile transformation of nanocrystalline TiO<sub>2</sub>: an XRD and Raman spectroscopy investigation. *Cryst Eng Comm* 13:5055–5061
41. Peng X, Chen A (2004) Aligned TiO<sub>2</sub> nanorod arrays synthesized by oxidizing titanium with acetone. *J Mater Chem* 14:2542–2548
42. Beati AAGF, Reis RM, Rocha RS, Lanza MRV (2012) Development and evaluation of a pseudoreference Pt/Ag/AgCl electrode for electrochemical systems. *Ind Eng Chem Res* 51:5367–5371
43. Yang SH, Lin Y, Song XF, Zhang P, Gao L (2015) Covalently coupled ultrafine H-TiO<sub>2</sub> nanocrystals/nitrogen-doped graphene hybrid materials for high-performance supercapacitor. *ACS Appl Mater Interfaces* 7:17884–17892
44. Santiago FF, Mora-Sero I, Garcia-Belmonte G, Bisquert J (2003) Cyclic voltammetry studies of nanoporous semiconductors. Capacitive and reactive properties of nanocrystalline TiO<sub>2</sub> electrodes in aqueous electrolyte. *J Phys Chem B* 107:758–768
45. Wu H, Li D, Zhu X, Yang C, Liu D, Chen X, Song Ye LL (2014) High-performance and renewable supercapacitors based on TiO<sub>2</sub> nanotube array electrodes treated by an electrochemical doping approach. *Electro Acta* 116:129–136
46. Li M, Zhou M, Wen QZ, Zhang XY (2017) Flower-like NiFe layered double hydroxides coated MnO<sub>2</sub> for high-performance flexible supercapacitors. *J of Ener Stor* 11:242–248
47. Xiao J, Wan L, Yang S, Xiao F, Wang S (2014) Design hierarchical electrode with highly conductive NiCo<sub>2</sub>S<sub>4</sub> nanotube performance arrays grown on carbon fiber paper for high-performance Pseudocapcitors. *Nano Lett* 14: 831–838
48. Liu LJ, Chen M, Zhang L, Jiang J, Yan J, Huang Y, Lin J, Fan JH, Shen XZ (2014) A flexible alkaline rechargeable Ni/Fe battery based on graphene foam/carbon nanotubes hybrid film. *Nano Lett* 14:7180–7187
49. Liu B, Liu B, Wang Q, Wang X, Xiang Q, Chen D, Shen G (2013) New energy storage option: toward ZnCo<sub>2</sub>O<sub>4</sub> nanorods/nickel foam architectures for high-performance supercapacitors. *ACS Appl Mater Inter*. 5:10011–10017
50. Tang Z, Tang CH, Gong H (2012) A high energy density asymmetric supercapacitor from nano-architected Ni (OH)<sub>2</sub>/carbon nanotube electrodes. *Adv Funct Mater* 22:1272–1278
51. Zhang Q, Xu WW, Sun J, Pan ZH, Zhao JX, Wang X, Zhang J, Man P, Guo JB, Zhou ZY, He B, Zhang ZX, Li QW, Zhang YG, Xu L, Yao Y (2017) Constructing ultrahigh-capacity zinc–nickel–cobalt oxide @ Ni(OH)<sub>2</sub> Core–Shell nanowire arrays for high-performance coaxial fiber-shaped asymmetric supercapacitors. *Nano Lett* 17:7552–7560



52. Zhi J, Zhao W, Lin TQ, Huang F (2017) Boosting supercapacitor performance of TiO<sub>2</sub> nanobelts by efficient nitrogen doping. *Chem Electro Chem* 4:2328–2335
53. Di J, Fu XC, Zheng H, Jia Y (2015) H-TiO<sub>2</sub>/C/MnO<sub>2</sub> nanocomposite materials for high-performance supercapacitors. *J Nano Res* 17:255–266
54. Barnard SA, Curtiss AL (2005) Prediction of TiO<sub>2</sub> nanoparticle phase and shape transitions controlled by surface chemistry. *Nano Lett* 5:1261–1266
55. Barnard SA, Zapol P (2004) Predicting the energetics, phase stability, and morphology evolution of faceted and spherical anatase nanocrystals. *J Phys Chem B* 108:18435–18440
56. Barnard SA, Zapol P, Curtiss AL (2005) Anatase and rutile surfaces with adsorbates representative of acidic and basic conditions. *Surf Sci* 582:173–188
57. Hercule MK, Wei Q, Khan MA, Zhao LY, Tian CX, Mai QL (2013) Synergistic effect of hierarchical nanostructured MoO<sub>2</sub>/Co(OH)<sub>2</sub> with largely enhanced pseudocapacitor cyclability. *Nano Lett* 13:5685–5691
58. Carrara S, Bavastrello V, Ricci D, Stura E, Nicolini C (2005) Improved nano composite materials for biosensor applications investigated by electrochemical impedance spectroscopy. *Sens Actu B* 109:221–226
59. Zhao H, Liu L, Vellacheri R, Lei Y (2017) Recent advances in designing and fabricating self-supported nanoelectrodes for supercapacitors. *Adv Sci* 4: 1700188–1700222

**Submit your manuscript to a SpringerOpen<sup>®</sup> journal and benefit from:**

- ▶ Convenient online submission
- ▶ Rigorous peer review
- ▶ Open access: articles freely available online
- ▶ High visibility within the field
- ▶ Retaining the copyright to your article

---

Submit your next manuscript at ▶ [springeropen.com](https://www.springeropen.com)

---